

Analytical, experimental, and Monte Carlo system response matrix for pinhole SPECT reconstruction

Pablo Aguiar^{a)}

Fundación Ramón Domínguez, Medicina Nuclear, CHUS, Spain and Grupo de Imaxe Molecular, IDIS, Santiago de Compostela 15706, Spain

Francisco Pino

Unitat de Biofísica, Facultat de Medicina, Universitat de Barcelona, Spain and Servei de Física Mèdica i Protecció Radiològica, Institut Català d'Oncologia, Barcelona 08036, Spain

Jesús Silva-Rodríguez

Fundación Ramón Domínguez, Medicina Nuclear, CHUS, Santiago de Compostela 15706, Spain

Javier Pavía

Servei de Medicina Nuclear, Hospital Clínic, Barcelona, Spain; Institut d'Investigacions Biomèdiques August Pi i Sunyer (IDIBAPS), Spain; and CIBER en Bioingeniería, Biomateriales y Nanomedicina (CIBER-BBN), Barcelona 08036, Spain

Doménec Ros

Unitat de Biofísica, Facultat de Medicina, Casanova 143, Spain; Institut d'Investigacions Biomèdiques August Pi i Sunyer (IDIBAPS), Spain; and CIBER en Bioingeniería, Biomateriales y Nanomedicina (CIBER-BBN), Barcelona 08036, Spain

Álvaro Ruibal

Servicio Medicina Nuclear, CHUS, Spain; Grupo de Imaxe Molecular, Facultade de Medicina (USC), IDIS, Santiago de Compostela 15706, Spain; and Fundación Tejerina, Madrid, Spain

Ziad El Bitar

Université de Strasbourg, IPHC, 23 rue du Loess 67037 Strasbourg, France and CNRS, UMR7178, Strasbourg 67037, France

(Received 11 October 2013; revised 24 January 2014; accepted for publication 9 February 2014; published 3 March 2014)

Purpose: To assess the performance of two approaches to the system response matrix (SRM) calculation in pinhole single photon emission computed tomography (SPECT) reconstruction.

Methods: Evaluation was performed using experimental data from a low magnification pinhole SPECT system that consisted of a rotating flat detector with a monolithic scintillator crystal. The SRM was computed following two approaches, which were based on Monte Carlo simulations (MC-SRM) and analytical techniques in combination with an experimental characterization (AE-SRM). The spatial response of the system, obtained by using the two approaches, was compared with experimental data. The effect of the MC-SRM and AE-SRM approaches on the reconstructed image was assessed in terms of image contrast, signal-to-noise ratio, image quality, and spatial resolution. To this end, acquisitions were carried out using a hot cylinder phantom (consisting of five fillable rods with diameters of 5, 4, 3, 2, and 1 mm and a uniform cylindrical chamber) and a custom-made Derenzo phantom, with center-to-center distances between adjacent rods of 1.5, 2.0, and 3.0 mm.

Results: Good agreement was found for the spatial response of the system between measured data and results derived from MC-SRM and AE-SRM. Only minor differences for point sources at distances smaller than the radius of rotation and large incidence angles were found. Assessment of the effect on the reconstructed image showed a similar contrast for both approaches, with values higher than 0.9 for rod diameters greater than 1 mm and higher than 0.8 for rod diameter of 1 mm. The comparison in terms of image quality showed that all rods in the different sections of a custom-made Derenzo phantom could be distinguished. The spatial resolution (FWHM) was 0.7 mm at iteration 100 using both approaches. The SNR was lower for reconstructed images using MC-SRM than for those reconstructed using AE-SRM, indicating that AE-SRM deals better with the projection noise than MC-SRM.

Conclusions: The authors' findings show that both approaches provide good solutions to the problem of calculating the SRM in pinhole SPECT reconstruction. The AE-SRM was faster to create and handle the projection noise better than MC-SRM. Nevertheless, the AE-SRM required a tedious experimental characterization of the intrinsic detector response. Creation of the MC-SRM required longer computation time and handled the projection noise worse than the AE-SRM.

Nevertheless, the MC-SRM inherently incorporates extensive modeling of the system and therefore experimental characterization was not required. © 2014 Author(s). All article content, except where otherwise noted, is licensed under a Creative Commons Attribution 3.0 Unported License. [<http://dx.doi.org/10.1118/1.4866380>]

Key words: pinhole SPECT, iterative reconstruction, ray-tracing techniques, Monte Carlo simulation, system response matrix

1. INTRODUCTION

Molecular imaging techniques play a valuable role in preclinical areas such as drug development, gene expression, and nanoparticle-based cell therapy monitoring.¹⁻⁶ In particular, single photon emission computed tomography (SPECT) has become an essential tool in this field⁷ thanks to its ability to provide images of peptides, antibodies, and hormones labeled with Technetium (Tc-99m) and other radio-isotopes. The relatively slow diffusion of these molecules allows the imaging of processes such as cell division, infection, and inflammation. Furthermore, pinhole SPECT provides high resolution images thanks to the use of pinhole instead of parallel-hole collimators. This, enables us to achieve submillimeter spatial resolution when the object is positioned close to the pinhole.⁸⁻¹¹ This advantage comes at the expense of a reduced field of view which restricts the clinical use of these imaging systems.

On the other hand, tomographic reconstruction methods play a vital role in the quality of the images, and algorithms that include accurate description of the acquisition process can lead to high spatial resolution images. Iterative statistical reconstruction algorithms have become standard procedures in SPECT, offering the possibility of improved image quality with respect to analytical methods.¹²⁻¹⁴ The most common statistical reconstruction method is the maximum likelihood expectation maximization (ML-EM),¹⁵ and its accelerated version, the ordered subsets expectation maximization (OS-EM).¹⁶ The key element of this statistical reconstruction algorithm is the system response matrix (SRM), which models the relationship between the image and the projection space. In recent years, different methods to obtain the SRM have been reported, those that model the SRM analytically, with or without experimental characterization, and those that make use of Monte Carlo (MC) simulation.

In the analytical approach, the elements of the SRM are calculated using geometrical ray-tracers¹⁷⁻¹⁹ so that only the effects of the geometrical component are considered. The geometrical contribution computes detected photons by considering photon propagation in a rectilinear path as they travel in a homogeneous medium and through the point-aperture of the pinhole collimator. In order to include other effects such as intrinsic detector response, finite aperture, and septal penetration, the SRM has to be factorized into several submatrices,²⁰ each of which is related to a relevant aspect of the image formation.^{21,22} The intrinsic detector response contribution computes detected photons by considering photon interactions within the detector. The finite aperture

effect takes into account that the pinhole collimator is actually a finite circular aperture. The septal penetration contribution computes detected photons coming from the pinhole collimator edges. All this requires a laborious characterization of the system through experimental measurements, so that the system response is incorporated into the reconstruction process using different point spread function (PSF) models.^{23,24}

When modeling is carried out using MC simulations, the resulting elements of the SRM include a full system response, thus presenting an alternative to factorization and experimental characterization. To date, the robustness of these techniques for SPECT has already been demonstrated for both parallel²⁵⁻²⁸ and pinhole collimators,^{29,30} but implementation involves a challenging computational task since pinhole SPECT simulations are time consuming. Because of this, several variance reduction methods based on forced detection techniques have been put forward.³¹⁻³³ These techniques are based on forcing each emitted photon to a circular area in the pinhole aperture, which considerably increase the number of detected events.

In summary, analytical computation of the SRM is fast but requires an experimental characterization of the system to include other effects in addition to the geometrical component. On the other hand, computation of the SRM by using MC simulations allows a full characterization without experimental measurements, but it is very time consuming. Nowadays, although it is well known that accurate modeling of the SRM is crucial in statistical reconstruction, it is still unclear which is the most suitable approach for each application. In a previous work,³⁴ we compared different analytical techniques and MC computation of the SRM for 3D PET reconstruction. Our findings showed that MC computation of the SRM yields small improvements in terms of contrast and spatial resolution with respect to the analytical approach.

The aim of the present work is to assess the performance of different approaches to the SRM calculation in low magnification pinhole SPECT reconstruction. The SRM was computed in line with two approaches, based on (1) Monte Carlo simulation (MC-SRM) and on (2) analytical techniques in combination with an experimental characterization (AE-SRM).

2. MATERIALS AND METHODS

2.A. Pinhole SPECT scanner

Our work focuses on a pinhole SPECT system³⁵ consisting of a rotating flat detector with a monolithic scintillator crystal (Cesium Iodine, CsI) of $50 \times 50 \times 4 \text{ mm}^3$ coupled to a Hamamatsu H8500 position sensitive photomultiplier (PS-PMT) and 1 mm diameter tungsten pinhole with a knife-edge

90° aperture.³⁶ The gamma camera is attached to a variable radius system so that sensitivity and spatial resolution can be optimized by adjusting the radius of rotation to the size of the object.

2.B. System response matrix

As stated above, the key element of any statistical reconstruction algorithm is the SRM. Each element a_{ij} of this matrix corresponds to the probability that a photon emission in voxel j results in the detection of an event by detector element i . Therefore, if q_j is the original radioactivity distribution in voxel j and n_i is the statistical noise in the projection, the measured projection p_i can be described by the following equation:

$$p_i = \sum_{j=1}^J a_{ij} q_j + n_i, \quad (1)$$

where $i \in [1, I]$, $j \in [1, J]$, and I and J are the total number of projection bins and the total number of image voxels, respectively.

2.C. Monte Carlo SRM

MC simulations were used to obtain an accurate description of all the phenomena involved in the SPECT imaging process, which relates the activity distribution to the photons collected by the detector. The complete SRM was obtained without factorization:

- **GEANT4 simulations:** The complete system response was obtained by using GEANT4 (v9.4) simulations³⁷ of a cylinder equal in size to the field of view (FOV) and filled with a Tc-99m solution of uniform activity concentration.^{25,29} Simulation took into account most of the physical phenomena involved in radiation-matter interactions, including the gamma emission, pinhole collimation, and gamma detection. Thus, photoelectric effect, and Compton and Rayleigh scatter were modeled for gamma rays whereas multiple scattering and ionization were modeled for electrons. Characteristic x rays of tungsten were not included because their contribution to the energy window centered on 140 keV is negligible. To overcome the problem of large computing time, parallel simulations were performed on a computing grid composed of 1000 computing elements. The intrinsic response of the detector was modeled by considering two contributions: photon interactions within the detector and optical transport. The contribution of photon interactions was considered by tracking the photons within the detector, recording the Compton interactions for each photon in order to compute the energy-weighted centroid and total energy deposited. The tracking for optical photons was modeled by applying a Gaussian blurring of 1.6 mm FWHM.
- **Variance reduction techniques:** Methods for variance reduction were implemented into GEANT4 based on forced detection, so as to obtain almost noise-free simu-

lations within a reasonable time. Thus, accelerated MC simulations³⁸ were carried out by forcing the direction of photons toward a circular area centered on the pin-hole collimator. The detected photons were weighted to compensate for the fact that emission was constrained within a limited solid angle. The number of simulated histories was 2×10^4 (realizations) in 60 projections and 10^6 photons per projection, resulting in 12×10^{11} total simulated histories and finally 10^8 detected events.

2.D. Analytical and experimental SRM

Computation of the different elements of the SRM can be a very tedious task, due to the large size of the matrix. To facilitate the computation, the complete matrix was divided into several submatrices,²⁰ each related to a relevant aspect in the image formation process:

- **Geometrical component:** This was obtained using a fast Siddon ray-tracer.¹⁷ Each element of the matrix was computed as the length of intersection between lines (bin-voxel) and individual voxels.
- **Intrinsic detector response:** An experimental characterization of the intrinsic spatial detector response was carried out through measurements using a pencil beam. This beam was created by collimating a source using a lead cylinder 30 cm long and 2 mm thick, with its ends closed by two circular lead covers, 4 mm thick. The source was placed on the inner side of one of the covers, while a hole of 0.5 mm in diameter was drilled in the opposite cover. A set of intrinsic detector responses was obtained for different angles of incidence and stored in LUTs according to incidence angles (from 0° to 46° in steps of 2°) and polar angles (from 0° to 360° in steps of 2°).
- **Finite aperture and septal penetration:** Analytical models of finite aperture and septal penetration were also included. To this end, an equivalent aperture diameter yielding a geometric resolution equal to the total resolution of the real pinhole was considered.³⁹ Scatter in the collimator was not considered.

Finally, each element of the SRM was generated as the convolution of a projected voxel (including the geometrical component, finite aperture and septal penetration) with the intrinsic detector response corresponding to the incidence and polar angle between the ray and detector surface (from LUTs).

2.E. Image reconstruction

Once the SRM was obtained, the maximum likelihood expectation maximization algorithm (ML-EM),¹⁵ with its accelerated version, the ordered subsets expectation maximization,¹⁶ was used for the reconstruction. The image is obtained from comparisons between estimated and measured projection data, in such a way that each element q_j of the image at iteration $k + 1$ is updated in accordance with the

following equation:

$$q_j^{k+1,n} = \frac{q_j^k}{s_j^n} \sum_{i=1}^{I_n} a_{ij} \frac{p_i}{\hat{p}_i}. \quad (2)$$

An iteration of algorithm is thus defined as a single pass through all the subsets, where a_{ij} is an element of the SRM; $i \in [1, I_n]$ is the projection bin; I_n is the number of projection bins in the subset n ($n \in [1, SB]$, SB is the number of subsets); $j \in [1, J]$ is the image voxel, being J the number of image voxels; p_i is the measured projection data; \hat{p}_i is the estimated projection data which is obtained after forward projection of the estimated image at iteration k as

$$\hat{p}_i \equiv \sum_{j=1}^J a_{ij} q_j^k. \quad (3)$$

s_j^n is an element of the sensitivity image \mathbf{s} , which represents the probability that a photon emission occurring in voxel j is detected. It can be obtained by adding all projection bin values of the subset n of the SRM in accordance with

$$s_j^n \equiv \sum_{i=1}^{I_n} a_{ij}. \quad (4)$$

2.F. Mechanical misalignments and calibration

The mechanical misalignments and system response modeling are closely related topics in pinhole SPECT imaging, and a reconstruction method implemented without the ability to correct for geometric misalignments is of little interest in practical molecular imaging studies. That is why the reconstruction of pinhole SPECT data requires a correct description of the acquisition geometry and this information needs to be included in both the analytical calculations and MC simulations.

2.F.1. Definition of mechanical misalignments

The object is defined in the xyz system, with the z axis along the rotation axis (Fig. 1) so that for a given rotation angle θ (angle between the detector surface and the x axis), a point (x, y) of the activity distribution $A(x, y, z)$ is projected through the pinhole with d diameter onto the point (u, v) of the detector. The origin of the uv system is perpendicular to the projection of the origin of the xyz system on the detector. To consider mechanical misalignments, the geometry of the acquisition can be completely described using seven calibration parameters.⁴⁰ The radius (r), is the distance between the center of the hole and the center of rotation. The focal length (f) is the distance between the center of the hole and the detector. The mechanical offset (m) is the distance between the rotation axis and the pinhole projection ray orthogonal to the detector. The *tilt* angle is the angle between the detector and the rotation axis. The *twist* angle is the angle describing a rotation of the detector around an axis parallel to the central ray. The electrical shifts (e_u and e_v) account for a collective trans-

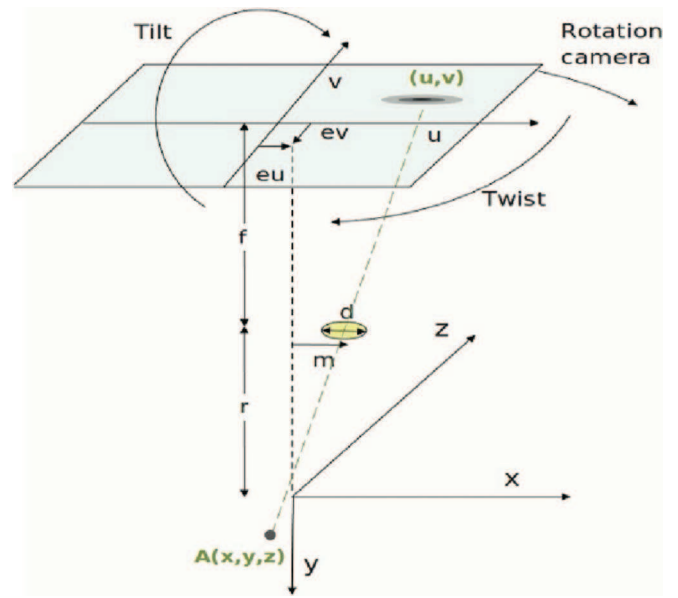


FIG. 1. Rotating-camera geometry, where z axis is the rotation axis of the system, and $A(x, y, z)$ is the activity distribution defined in the xyz system and projected into the uv system through the pinhole (d diameter).

lation of the projection image caused by a drift of the detector hardware.

2.F.2. Calibration acquisition

The seven calibration parameters (r, f, m, e_u, e_v , and *tilt* and *twist* angles) that describe the geometry of the acquisition can be obtained from a 60 projections acquisition of a three-point Tc-99m phantom.⁴⁰ To this end, we minimize a penalty function defined as the sum of quadratic differences of the coordinates of the projected centers of the point sources and the experimentally acquired centers.

2.G. MC-SRM versus AE-SRM

2.G.1. System PSFs

A comparison of the different spatially variant point spread functions (PSF) incorporated into the reconstruction was carried out. To this end, different projected point sources were obtained using the projectors estimated from MC-SRM and AE-SRM. The mechanical misalignments obtained from the calibration acquisition were included into both SRM models. Furthermore, scans of different point sources were also carried out, yielding profiles of the projected sources at different distances and angles from the pinhole collimator. The profiles corresponded to the projected points placed at distances greater (27.2, 29.1, and 26.4 mm) and smaller (17.9, 16.6, and 18.1 mm) than the radius of rotation, and for three different incidence angles (4° , 13° and 20°).

2.G.2. Contrast and signal-to-noise ratio (SNR)

Contrast and SNR were evaluated using a hot cylinder phantom made of polymethylmethacrylate with internal

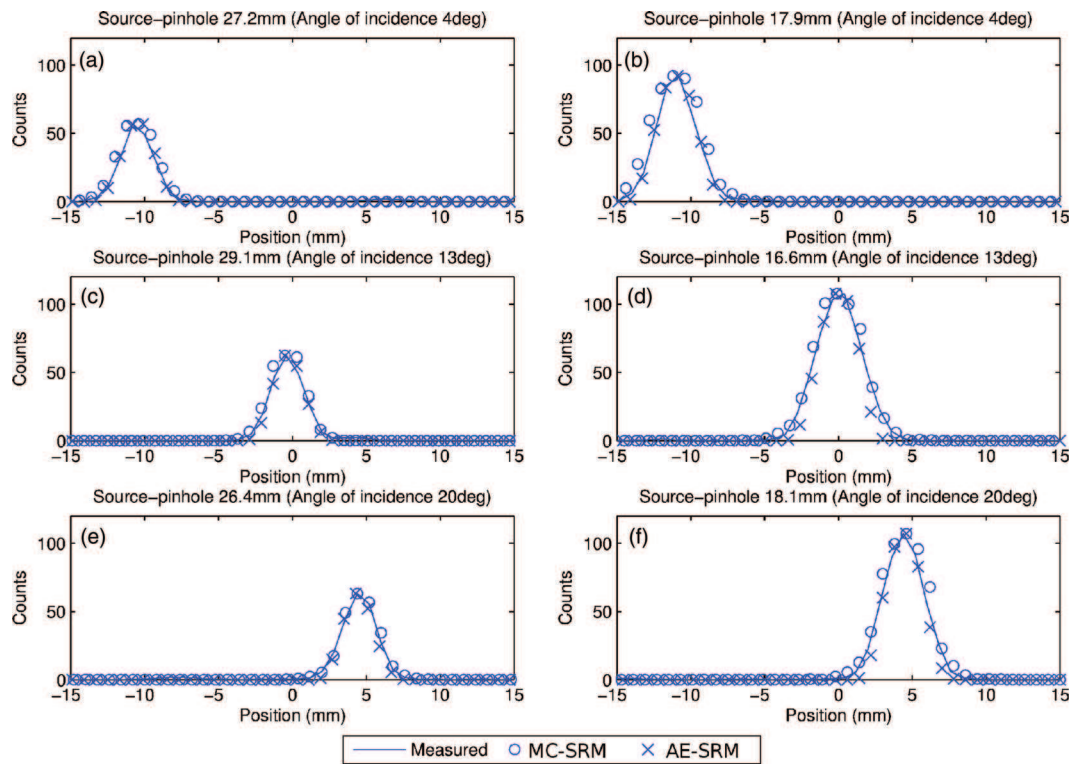


FIG. 2. PSFs for point sources placed at distances greater (27.2, 29.1, and 26.4 mm) and smaller (17.9, 16.6, and 18.1 mm) than the radius of rotation, and for three incidence angles (4° , 13° , and 20°). The transverse profiles were obtained through projected points using MC-SRM and AE-SRM. Experimental profiles are also shown for comparison.

dimensions of 50 mm in length and 30 mm in diameter. The phantom was composed of a fillable cylindrical chamber 30 mm in diameter and 30 mm long (uniform section). The remaining length (20 mm) of phantom was solid with five fillable rods placed at 7 mm from the center with diameters of 5, 4, 3, 2, and 1 mm (rod section). A 150 min scan time study was carried out with rod and uniform sections filled with 37 MBq/ml (1 mCi/ml) of a Tc-99m solution.

The image contrast was defined as

$$\text{contrast} = \frac{\bar{q}_{roi} - \bar{q}_{bg}}{\bar{q}_{roi} + \bar{q}_{bg}}, \quad (5)$$

where \bar{q}_{roi} is the mean value in a region-of-interest (ROI) drawn within the cylinders. These ROIs had volumes of 3.1, 12.6, 28.3, 50.3, and 78.5 mm³, respectively, and covered a length of 4 mm; \bar{q}_{bg} is the mean value of the background. The volume of the background ROI was 113.1 mm³ (6 mm diameter) and also covered a length of 4 mm. In an ideal reconstruction, contrast should be 1.

The uniform region of the hot cylinder phantom was also used to characterize image noise. Uniform slices were used to obtain the SNR ratio as the quotient between the mean value to the standard deviation, obtained in a transaxial central ROI, 22.5 mm in diameter. The diameter was chosen to represent 75% of the phantom diameter (30 mm).

2.G.3. Derenzo phantom

A 60 min scan time study of a custom-made Derenzo phantom was carried out. The hot rods had an inner diameter of

0.3 mm and the center-to-center distances between adjacent rods were 1.5, 2.0, and 3.0 mm in each of the three sections of the phantom. Acquisition parameters were 60 views (angle step: 6°) and 150×150 projection sampling (bin size:

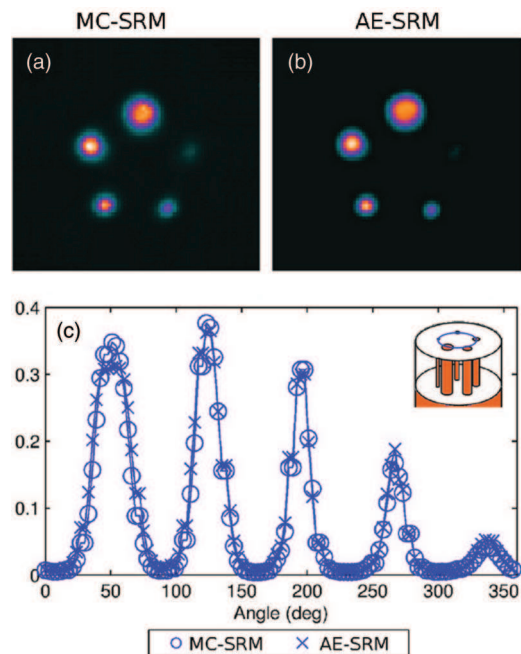


FIG. 3. Reconstructed images and profiles from the hot cylinder phantom by using MC-SRM and AE-SRM: reconstructed images of the hot rod section by using MC-SRM (a), AE-SRM (b), and circular profiles (c).

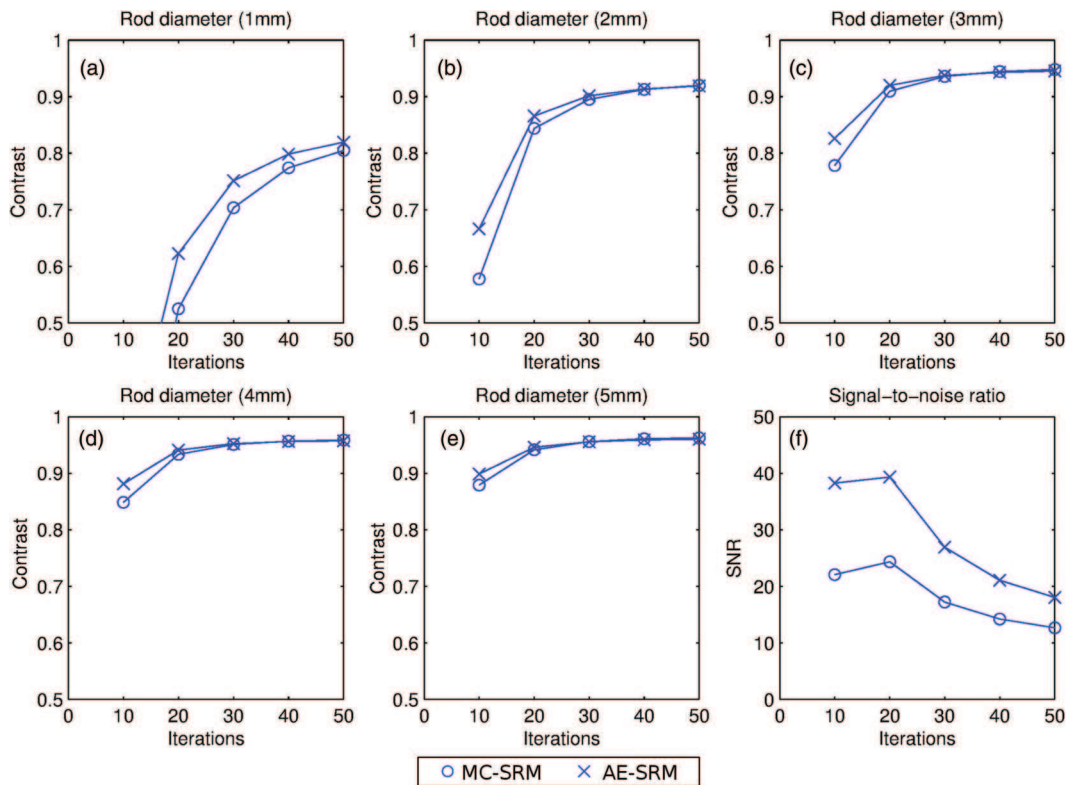


FIG. 4. Contrast versus number of iterations for the different cylinder diameters (a)–(e), obtained from reconstructed images by using MC-SRM and AE-SRM. SNR versus number of iterations from reconstructed images by using MC-SRM and AE-SRM (f).

0.26 mm). Reconstructed images of the Derenzo phantom were obtained using 5 subsets, 400 iterations, and a voxel size of $0.2 \times 0.2 \times 0.8$ mm (an iteration of this algorithm was defined as a single pass through all the subsets).

2.G.4. Spatial resolution

The previous acquisition was also used to estimate the spatial resolution of the system. Thus, the rods of the section with center-to-center distances between adjacent rods of 3.0 mm (with rods sufficiently apart) were used to obtain the spatial resolution as the FWHM (mm) of the fitted Gaussian. These rods were placed at distances from the center FOV of 2.3, 3.8, 5.1, and 5.2 mm.

2.G.5. Matrix file size and computing time

Aimed at evaluating MC-SRM and AE-SRM in relation to their computational requirements, both approaches were compared in terms of file sizes and computing time.

3. RESULTS

3.A. System PSFs

Figure 2 shows the transverse profiles obtained through the projected points using MC-SRM and AE-SRM models. The transverse profiles from experimental measurements are also shown for comparison. First, our comparison indicates

that both SRM models are in good agreement with measured data, thereby demonstrating the accuracy of both models of system PSF. Nevertheless, a detailed analysis of the profiles shows some relevant issues that should be highlighted. The PSFs obtained from point sources placed at distances greater than the radius of rotation (27.2, 29.1, and 26.4 mm) show a better agreement than those obtained from point sources placed at smaller distances (17.9, 16.6, and 18.1 mm). In this case, PSFs obtained from the AE-SRM model were slightly narrower than those corresponding to experimental measurements, whereas PSFs obtained from the MC-SRM were slightly wider than those obtained experimentally. The latter is particularly important for an angle of incidence of 4° , which corresponds to a point at the edge of the detector. A comparison in terms of FWHM and FWTM showed notable differences. Thus, the mean bias between MC-SRM and experimental PSFs was 0.32 mm in FWHM and 0.27 mm in FWTM. The mean bias between AE-SRM and experimental PSFs was -0.13 mm in FWHM and -0.60 mm in FWTM. These results demonstrate that PSF is slightly overestimated in terms of FWHM and FWTM when using MC-SRM and that AE-SRM causes FWTM to be significantly lower than the experimental measurements.

It can be seen that the projection for small angles of incidence (close to the perpendicular direction, for example, 4°) corresponds to a point at the edge of the detector, not at the center of the detector, as would be expected. This can be explained by mechanical misalignments. The geometrical

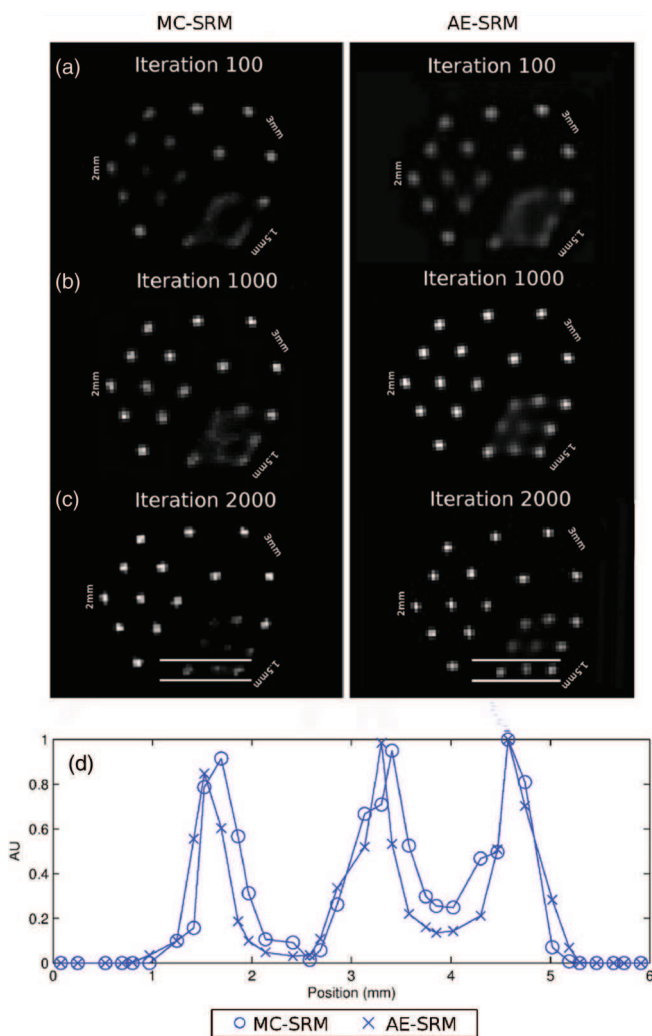


FIG. 5. Derenzo reconstructions using MC-SRM (left) and AE-SRM (right), for iteration 100 (a), 200 (b), and 2000 (c). Profiles through the rods of section with center-to-center distances of 1.5 mm are also shown (d).

parameters obtained from the calibration acquisition were the radius of rotation (22.5 mm), focal length (33.1 mm), mechanical offset (3.1 mm), tilt angle (0.75°), twist angle (0.69°), transverse (-4.5 mm), and axial shift (2.3 mm). It is noteworthy that an excellent agreement exists in the position of each projected point source (measured, MC-SRM and AE-SRM), demonstrating the correct implementation of the different calibration parameters.

3.B. Contrast and signal-to-noise-ratio

Figure 3 shows transaxial slices and profiles of hot rod section reconstructions using MC-SRM and AE-SRM. The maximum number of iterations for both cases was 50. The use of a higher number of iterations resulted in ring effect artifacts without increasing the contrast. A visual comparison of the reconstructed images in Fig. 3 shows a similar image quality for both models under investigation. Thus, both models allow us to see clearly all rods with diameter exceeding than 1 mm but not so clearly the 1 mm diameter rod. The profiles also show

an excellent agreement between the MC-SRM and AE-SRM reconstructions.

Figure 4 shows a quantitative comparison of the previous images in terms of contrast and SNR. As expected, contrast increases with the number of iterations and with the rod diameter. A similar quantitative performance can be observed for both models, showing similar contrast values for all rods after 50 iterations. On the whole, very high contrast values (>0.9) were obtained for rod diameters greater than 1 mm and relatively high contrast values (>0.8) for the rod diameter of 1 mm. Figure 4 shows that convergence for MC-SRM is slightly slower, especially for the rod diameter of 1 mm. Figure 4 also provides a comparison between SNR, estimated from the uniform section of the images reconstructed using MC-SRM and AE-SRM approaches. We can see that for the same number of iterations, the images reconstructed using MC-SRM exhibit higher noise.

3.C. Derenzo phantom

Figure 5 shows reconstructed images (iterations 100, 200, and 2000) from the custom-made Derenzo phantom acquisition using MC-SRM and AE-SRM. The rods in sections with center-to-center distances of 2.0 and 3.0 mm can be distinguished at iterations 100 and 200. Nevertheless, rods in the section with center-to-center distances of 1.5 mm are very fuzzy, from both MC-SRM and AE-SRM reconstructions. A proper visualization of these rods required many iterations, resulting in an increase in the statistical noise. An interesting difference between MC-SRM and AE-SRM was found at this point. Although all the rods could be distinguished at iteration 2000 using both models, statistical noise increased faster for MC-SRM. Hence, reconstructed images are noisier than those obtained by using AE-SRM. This led to jagged MC-SRM profiles through three rods in this section, asymmetries in some rods and nonzero background.

3.D. Spatial resolution

The section of the custom-made Derenzo phantom with center-to-center distances of 3.0 mm was used to estimate the averaged spatial resolution values at different distances from the center of FOV, for MC-SRM and AE-SRM reconstructions. Figure 6 shows radial (left) and tangential (right) FWHM at different distances from the center of FOV, for iteration 100 (a) and (b) and iteration 1000 (c) and (d). Spatial resolution values were improved for both approaches when the distance to the center of FOV increased, for radial and tangential FWHM. Furthermore, similar FWHM values were found for MC-SRM and AE-SRM at iteration 100. This is clearly derived from the FWHM values averaged over all distances to the center of FOV, and radial and tangential directions, which were 0.67 ± 0.02 and 0.68 ± 0.06 , for MC-SRM and AE-SRM, respectively. The spatial resolution for AE-SRM was slightly better than for MC-SRM at iteration 1000, showing FWHM values of 0.39 ± 0.02 and 0.47 ± 0.09 , respectively.

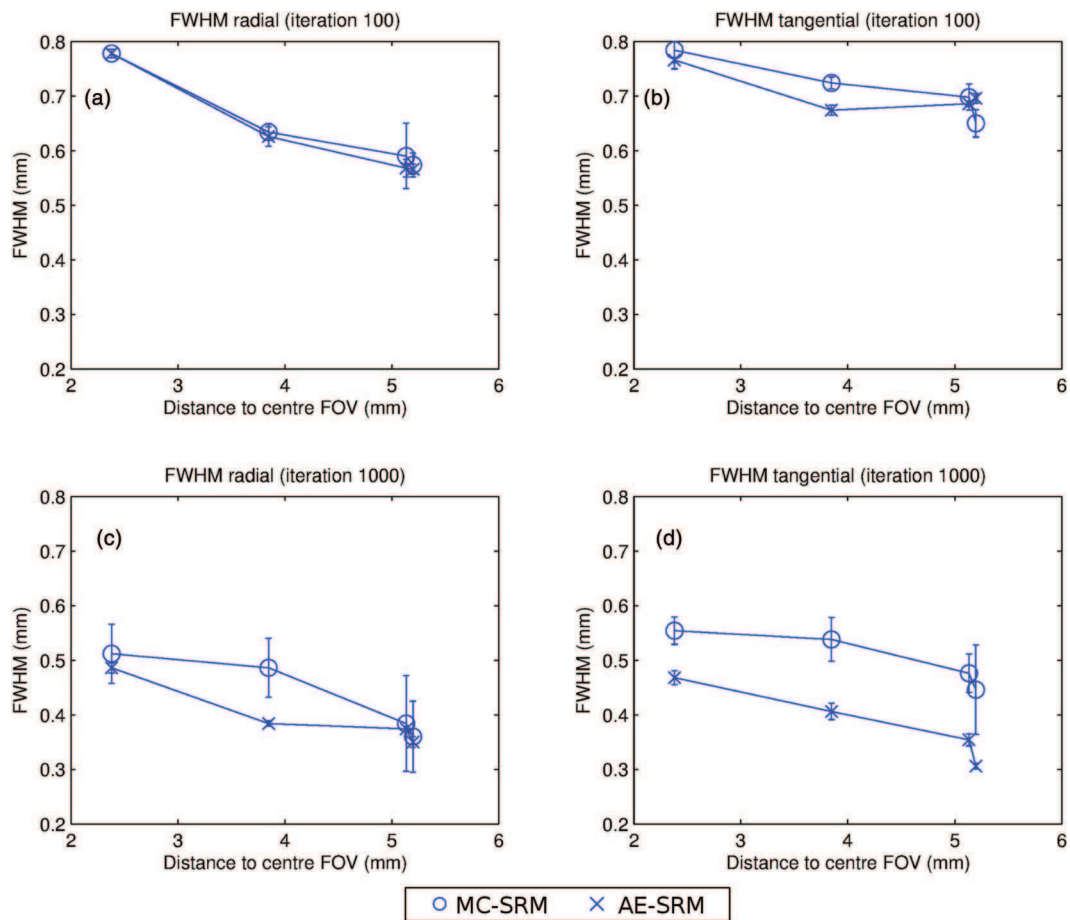


FIG. 6. Radial (left) and tangential (right) spatial resolution for rods placed at different distances from the center FOV (iteration 100 and 1000). The rods are placed at distances from the center FOV of 2.3, 3.8, 5.1, and 5.2 mm.

3.E. Matrix file size and computing time

Both MC-SRM and AE-SRM were precomputed and stored in sparse format. There were major differences, however between the computational requirements of the two techniques. MC-SRM calculations were carried out using a GRID computer cluster of about 1000 CPUs, whereas AE-SRM calculations were performed on a single CPU. The computing time for AE-SRM was 12 h on a single CPU and the file size containing the matrix was 11.6 Gb. The file size of the MC-SRM increased with the number of simulated photons and therefore with the computing time, converging to a file size of 12.1 GB for a computing time of 40 h on 1000 CPUs. As expected, the files for matrices from MC-SRM and AE-SRM were similar in size due to that the same sparse technique was used for compressing the matrix.

4. DISCUSSION AND CONCLUSIONS

We have assessed the effect on the final reconstructed images of the two main approaches to SRM calculation for iterative reconstruction in pinhole SPECT. In the first approach, the SRM was computed using MC-SRM. In the second approach, the SRM was computed using AE-SRM to include effects other than the geometrical component.

The comparison in terms of PSFs showed that both approaches (MC-SRM and AE-SRM) are in good agreement with the measured data. Nevertheless, some minor differences for point sources placed at distances smaller than the radius of rotation and for large incidence angles were found and need to be explained. First, PSFs derived from MC-SRM appear slightly wider than the measurements in terms of FWHM and FWTM, probably because of an overestimation of the optical transport effect (it seems that the PSF-shapes are similar). Second, it is clear that AE-SRM provides an acceptable approach in terms of FWHM but it is a poor approach for the PSF tails (FWTM) because the septal penetration model fails for small source-pinhole distances and large angles of incidence. The comparison of PSFs also shows that mechanical calibration methods are essential for tomographic reconstruction. This is evidenced by the fact that when mechanical misalignments exist, the projected points with small angles of incidence corresponded to point sources at the edge of the detector, and not at the center of the detector, as would be expected. In our case, the excellent agreement in the position of projected point sources after comparing MC-SRM and AE-SRM with experimental data, demonstrates the accurate implementation of corrections for various mechanical misalignments. As an additional result of this work, we currently have at our disposal well-validated tools for conducting

further studies on the effect of each of the calibration parameters on image quality.

The quantitative comparison in terms of image contrast shows that a high contrast can be obtained using both approaches (MC-SRM and AE-SRM), providing a very high contrast for rod diameters exceeding 1 mm and a relatively high contrast when the rod diameter is 1 mm. The comparison in terms of image quality and spatial resolution shows that all rods in the sections with center-to-center distances of 3.0, 2.0, and 1.5 mm could be distinguished on the basis of visual inspection and profile evaluation. Similar behavior was also found in terms of spatial resolution for both approaches, which showed that spatial resolution decreased in both transverse and radial directions from the center to the periphery of the FOV. It may be hypothesized that this spatial resolution dependence on source position is due to the differences in convergence speed in the different regions of the FOV. This was demonstrated using images reconstructed after a very high number of iterations from free-noise projections. These images showed that spatial resolution did not depend on the position in the FOV. In the experimental acquisitions, the number of iterations is limited because of the image noise and, as a consequence, differences in resolution can appear depending on the position of the point source in the FOV. Needless to say, the worst cases are in the center of the FOV.

Differences between the two approaches were found in image noise and hence for a high number of iterations. Comparison shows that a lower SNR is obtained from MC-SRM than from AE-SRM, thereby indicating that AE-SRM deals with projection noise better than MC-SRM. Similar spatial resolution values were obtained from MC-SRM and AE-SRM (0.7 mm) at iteration 100, but improved slightly for AE-SRM (0.4 mm) at iteration 1000. This leads us to state that statistical noise limits the spatial resolution for MC-SRM, due to the fact that it is not feasible to perform more iterations at acceptable levels of noise. The differences between the two approaches regarding SNR could be attributed to the MC-SRM projector inaccuracies, which could amplify the image noise. Nevertheless, the accurate implementation of the MC-SRM projector was demonstrated by reconstructing free-noise Derenzo projections, which provided similar spatial resolution values for MC-SRM and AE-SRM, even after many iterations. It should also be pointed out that the FWHM values are extremely low because a capillary placed in zero-background is the most favorable context for high iterations. Therefore, FWHM values obtained at iteration 1000 should not be regarded acceptable for the spatial resolution of the system. A reliable measurement of the spatial resolution of the system should be performed using a nonzero background, but this is outside the scope of the present work.

In summary, our findings show that both approaches constitute satisfactory solutions to the problem of calculating SRM for high performance pinhole SPECT reconstruction, showing high image quality and contrast values, and relatively good SNR and spatial resolution. While the AE-SRM approach is faster and handles projection noise better, it requires an experimental characterization of the intrinsic detec-

tor response to achieve a performance similar to that obtained using MC-SRM. The experimental characterization is a laborious and tedious task when trying to achieve the accuracy required in this case, and an extensive experimental background may be required, thus limiting its use to experienced groups. On the other hand, the MC-SRM approach is slower, does not handle the projection noise as well and its high performance computing requirements needs a GRID computer cluster, even after the implementation of complex variance reduction methods based on forced detection techniques. The implementation of the AE-SRM approach requires extensive experience with a suitable programming language and the MC-SRM approach can be performed using freely available packages, although some codes can also require knowledge of programming languages.

ACKNOWLEDGMENTS

This work was supported in part by Q-PET project (PI11/01806 - *Fondo de Investigaciones Sanitarias del Instituto de Salud Carlos III*), the *Spanish Ministry of Science and Innovation* (SAF2009-08076), and IQ-BRAIN project (10CSA918001PR - *Xunta de Galicia*). P. Aguiar was awarded a "Sara Borrell" fellowship (CD09/00291) by *Fondo de Investigaciones Sanitarias del Instituto de Salud Carlos III*. The authors also acknowledge the support of IPHC in providing computing resources on the Regional Grid Infrastructure (<http://www.grand-est.fr>).

^{a)} Author to whom correspondence should be addressed. Electronic mail: pablo.aguiar.fernandez@sergas.es

¹ A. Chatziioannou, "Molecular imaging of small animals with dedicated pet tomographs," *Eur. J. Nucl. Med. Mol. Imaging* **29**(1), 98–114 (2002).

² A. Jacobs, H. Li, A. Winkeler, R. Hilker, C. Knoess, A. Rueger, N. Galldiks, B. Schaller, J. Sobesky, and L. Kracht, "PET-based molecular imaging in neuroscience," *Eur. J. Nucl. Med. Mol. Imaging* **30**(7), 1051–1065 (2003).

³ J. Lewis, S. Achilefu, J. Garbow, R. Laforest, and M. Welch, "Small animal imaging: Current technology and perspectives for oncological imaging," *Eur. J. Cancer* **38**(16), 2173–2188 (2002).

⁴ R. Myers, "The biological application of small animal PET imaging," *Nucl. Med. Biol.* **28**(5), 585–593 (2001).

⁵ C. Xu, L. Mu, I. Roes, D. Miranda-Nieves, M. Nahrendorf, J. A. Ankrum, W. Zhao, and J. M. Karp, "Nanoparticle-based monitoring of cell therapy," *Nanotechnology* **22**(49), 494001 (2011).

⁶ G. Loudos, G. C. Kagadis, and D. Psimadas, "Current status and future perspectives of in vivo small animal imaging using radiolabeled nanoparticles," *Eur. J. Radiol.* **78**(2), 287–295 (2011).

⁷ S. R. Meikle, P. Kench, M. Kassiou, and R. B. Banati, "Small animal SPECT and its place in the matrix of molecular imaging technologies," *Phys. Med. Biol.* **50**(22), R45–R61 (2005).

⁸ T. Funk, P. Despres, W. C. Barber, K. S. Shah, and B. H. Hasegawa, "A multipinhole small animal SPECT system with submillimeter spatial resolution," *Med. Phys.* **33**(5), 1259–1268 (2006).

⁹ B. Vastenhouw and F. Beekman, "Submillimeter total-body murine imaging with U-SPECT-I," *J. Nucl. Med.* **48**(3), 487–493 (2007).

¹⁰ M. Freed, M. A. Kupinski, L. R. Furenlid, D. W. Wilson, and H. H. Barrett, "A prototype instrument for single pinhole small animal adaptive SPECT imaging," *Med. Phys.* **35**(5), 1912–1925 (2008).

¹¹ F. van der Have, B. Vastenhouw, R. M. Ramakers, W. Branderhorst, J. O. Krahe, C. Ji, S. G. Staelens, and F. J. Beekman, "U-SPECT-II: An ultra-high-resolution device for molecular small-animal imaging," *J. Nucl. Med.* **50**(4), 599–605 (2009).

- ¹²T. Frese, N. Rouze, C. Bouman, K. Sauer, and G. Hutchins, "Quantitative comparison of FBP, EM and Bayesian reconstruction algorithms for the IndyPET scanner," *IEEE Trans. Med. Imaging* **22**(2), 258–276 (2003).
- ¹³K. Thielemans, C. Tsoumpas, S. Mustafovic, T. Beisel, P. Aguiar, N. Dikaios, and M. W. Jacobson, "STIR: Software for tomographic image reconstruction release 2," *Phys. Med. Biol.* **57**(4), 867–883 (2012).
- ¹⁴B. M. Fuster, C. Falcon, C. Tsoumpas, L. Livieratos, P. Aguiar, A. Cot, D. Ros, and K. Thielemans, "Integration of advanced 3D SPECT modeling into the open-source STIR framework," *Med. Phys.* **40**(9), 092502 (6pp.) (2013).
- ¹⁵L. Shepp and Y. Vardi, "Maximum-likelihood reconstruction for emission tomography," *IEEE Trans. Med. Imaging* **1**, 113–121 (1982).
- ¹⁶H. Hudson and R. Larkin, "Accelerated image reconstruction using ordered subsets of projection data," *IEEE Trans. Med. Imaging* **13**(4), 601–609 (1994).
- ¹⁷R. Siddon, "Fast calculation of the exact radiological path length for a three-dimensional CT array," *Med. Phys.* **12**, 252–257 (1985).
- ¹⁸X. Wu, "An efficient anti-aliasing technique," *ACM Comput. Graph. Siggraph Conf. Proc.* **25**(4), 143–152 (1991).
- ¹⁹C. Schretter, "A fast tube of response ray-tracer," *Med. Phys.* **33**(12), 4744–4748 (2006).
- ²⁰J. Qi, R. Leahy, A. Chatzioannou, S. Cherry, and F. Farquhar, "High-resolution 3D Bayesian image reconstruction using the microPET small animal scanner," *Phys. Med. Biol.* **43**(7), 1001–1013 (1998).
- ²¹Y. Du and E. C. Frey, "Quantitative evaluation of simultaneous reconstruction with model-based crosstalk compensation for 99mTc/123I dual-isotope simultaneous acquisition brain SPECT," *Med. Phys.* **36**(6), 2021–2033 (2009).
- ²²N. Song, Y. Du, B. He, and E. C. Frey, "Development and evaluation of a model-based downscatter compensation method for quantitative I-131 SPECT," *Med. Phys.* **38**(6), 3193–3204 (2011).
- ²³F. van der Have, B. Vastenhouw, M. Rentmeester, and F. J. Beekman, "System calibration and statistical image reconstruction for ultra-high resolution stationary pinhole SPECT," *IEEE Trans. Med. Imaging* **27**(7), 960–971 (2008).
- ²⁴B. Feng, M. Chen, B. Bai, A. M. Smith, D. W. Austin, R. A. Mintzer, D. Osborne, and J. Gregor, "Modeling of the point spread function by numerical calculations in single-pinhole and multipinhole SPECT reconstruction," *IEEE Trans. Nucl. Sci.* **57**(1), 173–180 (2010).
- ²⁵D. Lazaro, Z. El Bitar, V. Breton, D. Hill, and I. Buvat, "Fully 3D Monte Carlo reconstruction in SPECT: A feasibility study," *Phys. Med. Biol.* **50**(16), 3739–3754 (2005).
- ²⁶J. Ouyang, G. El Fakhri, and S. C. Moore, "Fast Monte Carlo based joint iterative reconstruction for simultaneous 99mTc/123I SPECT imaging," *Med. Phys.* **34**(8), 3263–3272 (2007).
- ²⁷J. Ouyang, X. Zhu, C. M. Trott, and G. El Fakhri, "Quantitative simultaneous 99mTc/123I cardiac SPECT using MC-JOSEM," *Med. Phys.* **36**(2), 602–611 (2009).
- ²⁸M. Elschot, M. G. Lam, M. A. van den Bosch, M. A. Viergever, and H. W. de Jong, "Quantitative Monte Carlo-based 90Y SPECT reconstruction," *J. Nucl. Med.* **54**(9), 1557–1563 (2013).
- ²⁹Z. El Bitar, D. Lazaro, C. Coello, V. Breton, D. Hill, and I. Buvat, "Fully 3D Monte Carlo image reconstruction in SPECT using functional regions," *Nucl. Instrum. Methods Phys. Res. A* **569**(2), 399–403 (2006).
- ³⁰Z. El Bitar, R. H. Huesman, R. Boutchko, V. Bekaert, D. Brasse, and G. T. Gullberg, "A detector response function design in pinhole SPECT including geometrical calibration," *Phys. Med. Biol.* **58**(7), 2395–2411 (2013).
- ³¹M. Ljungberg and S. E. Strand, "Attenuation and scatter correction in SPECT for sources in a nonhomogeneous object: A Monte Carlo study," *J. Nucl. Med.* **32**, 1278–1284 (1991).
- ³²H. Wang, R. J. Jaszczak, and R. E. Coleman, "Monte carlo modeling of penetration effect for iodine-131 pinhole imaging," *IEEE Trans. Nucl. Sci.* **43**(6), 3272–3277 (1996).
- ³³M. Gieles, H. W. de Jong, and F. J. Beekman, "Monte Carlo simulations of pinhole imaging accelerated by kernel-based forced detection," *Phys. Med. Biol.* **47**(11), 1853–1867 (2002).
- ³⁴P. Aguiar, M. Rafecas, C. Falcon, J. Pavia, and D. Ros, "Geometrical and Monte Carlo projectors in 3D PET," *Med. Phys.* **37**(11), 5691–5702 (2010).
- ³⁵F. Pino, N. Roe, A. Orero, C. Falcon, S. Rojas, J. M. Benlloch, D. Ros, and J. Pavia, "Development of a variable-radius pinhole SPECT system with a portable gamma camera," *Rev. Esp. Med. Nucl.* **30**(5), 286–291 (2011).
- ³⁶M. M. Fernandez, J. M. Benlloch, J. Cerda, B. Escat, E. N. Gimenez, N. Gimenez, C. W. Lerche, J. Martinez, N. Pavon, F. Sanchez, and A. Sebastia, "A flat-panel-based mini gamma camera for lymph nodes studies," *Nucl. Instrum. Methods Phys. Res. A* **527**, 92–96 (2004).
- ³⁷S. Agostinelli *et al.*, "Geant4—A simulation toolkit," *Nucl. Instrum. Methods Phys. Res. A* **506**, 250–303 (2003).
- ³⁸Z. El Bitar, V. Breton, D. Hill, and I. Buvat, "Acceleration of fully 3D Monte-Carlo based system matrix computation for image reconstruction in small animal SPECT," *IEEE Trans. Nucl. Sci.* **58**(1), 121–132 (2011).
- ³⁹R. Accorsi and S. D. Metzler, "Analytic determination of the resolution-equivalent effective diameter of a pinhole collimator," *IEEE Trans. Med. Imaging* **23**(6), 750–763 (2004).
- ⁴⁰D. Beque, J. Nuyts, G. Bormans, P. Suetens, and P. Dupont, "Characterization of pinhole SPECT acquisition geometry," *IEEE Trans. Med. Imaging* **22**(5), 599–612 (2003).